Polymer−Peptide Conjugates Convert Amyloid into Protein Nanobundles through Fragmentation and Lateral Association

John W. Smith,[†] Xing Jiang,[‡] Hyosung An,[†,§] Alexander M. Barclay,[⊥] Giuseppe Licari,[‡] Emad Tajkhorshid,[‡,∥,⊥] Edwin G. Moore,[⊥] Chad M. Rienstra,*[,⊥] Jeffrey S. Moore,*[,†,‡,⊥] and Qian Chen*[,†,‡,§,⊥]

[†]Department of Materials Science and Engineering, [‡]Beckman Institute for Advanced Science and Technology, [§]Materials Research Laboratory, [⊥]Department of Chemistry, and [∥]Department of Biochemistry, University of Illinois, Urbana, Illinois 61801, United States

S Supporting Information

ABSTRACT: The assembly of proteins into amyloid fibrils has become linked not only with the progression of myriad human diseases, but also with important biological functions. Understanding and controlling the formation, structure, and stability of amyloid fibrils are therefore major scientific goals. Here we utilize electron microscopy-based approaches combined with quantitative statistical analysis to show how a recently developed class of amyloid modulators—multivalent polymer−peptide conjugates (mPPCs)—can be applied to control the structure and stability of amyloid fibrils. In doing so, we demonstrate that mPPCs are able to convert 40-residue amyloid β-fibrils into ordered nanostructures through a combination of fragmentation and bundling. Fragmentation is shown to be consistent with a model where the rate constant of fragmentation is independent of the fibril length, suggesting a local and specific interaction between fibrils and mPPCs. Subsequent bundling, which was previously not observed, leads to the formation of sheetlike nanostructures that are surprisingly much more uniform than the original fibrils. These nanostructures have dimensions independent of the molecular weight of the mPPC and retain the molecular-level ordering of amyloid fibrils. Overall, we reveal a quantitative and nanoscopic understanding of how mPPCs can be applied to control the structure and stability of amyloid and demonstrate approaches to elucidate nanoscale amyloid phase behavior in the presence of functional macromolecules and other modulators.

KEYWORDS: amyloid, polymer−peptide conjugates, protein electron microscopy, functional polymers, protein nanomaterials
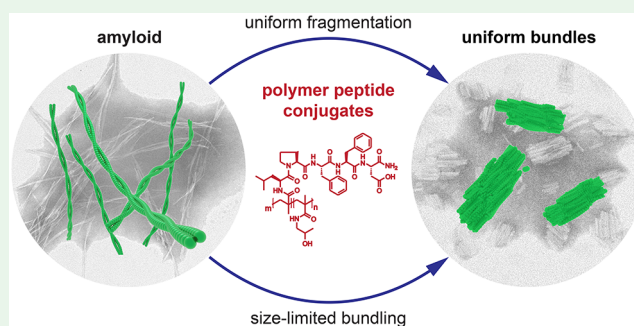
INTRODUCTION

The self-assembly of proteins into fibrils known as amyloid has become linked with both pathological and functional effects in biological systems. For example, amyloid formation from proteins like amyloid β (Aβ), α synuclein, and amylin has been implicated in the progression of Alzheimer's disease,[1,2] Parkinson's disease,[3] and type II diabetes,[4] whereas amyloid derived from curli, rodlin, and β-endorphin aid in such processes as the growth of bacterial biofilms,[5,6] the branching of fungal spores,[7,8] and the storage of neuropeptides.[9] Consequently, extensive research has been focused on understanding and modulating the structure, formation, and stability of amyloid fibrils.[2,10−12] In many investigations, ensemble spectroscopy techniques like thioflavin T (ThT) fluorescence assay[13−15] and circular dichroism (CD) spectroscopy,[15,16] which detect secondary structures characteristic of amyloid, can provide valuable insight. For example, these tools can be used to measure the rates of amyloid formation with or without molecular modulators and under various conditions and thereby reveal important details about both growth and

inhibitory mechanisms.[15,17] However, such tools generally reveal limited information about nanoscale phenomena that do not involve significant changes in the secondary structure or that involve heterogeneity, such as fragmentation,[18−21] tertiary structure changes,[8] or higher-order assembly and disassembly. Atomic force microscopy (AFM) has been the predominant tool to study the shape and size evolution of amyloid fibrils during such processes[19,20,22,23] but often at resolutions ≥10 nm, where primarily the exterior contours of amyloid structures are resolved. As a consequence, although many nanoscale processes play a critical role in the structure and phase behavior of amyloid[17,24] and can reduce or exacerbate the toxicity of amyloid fibrils,[18] they are not as well understood.
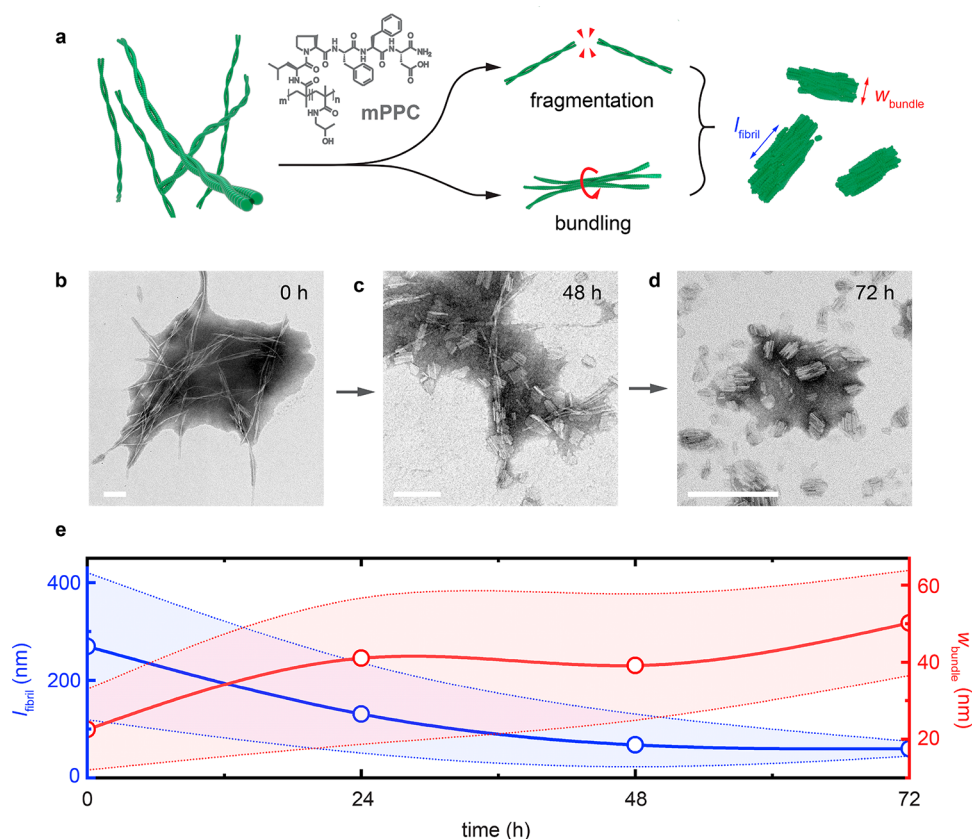
Figure 1. Overview of mPPC-induced $A\beta_{40}$ disassembly. (a) Schematic representation of the joint effects of fragmentation and bundling, induced by the introduction of mPPCs, to produce bundles of amyloid segments. (b−d) Representative time-lapse TEM images of disassembly 0, 48, and 72 h after the addition of mPPC. Additional examples and control samples without mPPC are presented in Figure S3. (e) Quantitative analysis of the fibril lengths (l_{fibril}) and bundle widths (w_{bundle}) over time. The shaded regions around the center line correspond to 1 standard deviation about the mean of the distribution. Scale bars: 200 nm.

Here we used an assortment of electron microscopy techniques to investigate how the structure and stability of 40-residue $A\beta$ ($A\beta_{40}$) fibrils can be controlled with multivalent polymer−peptide conjugates (mPPCs). Inspired by the way biological systems harness multivalent molecular interactions,[25−27] mPPCs consist of a hydrophilic polymer backbone bearing multiple copies of the "β-breaker" peptide LPFFD.[28,29] In previous works, it was shown that mPPCs can modulate both the growth and stability of amyloid, inhibiting the formation of $A\beta_{40}$ fibrils[13,23] and breaking down preformed $A\beta_{40}$ fibrils into sub-100-nm structures.[16] By virtue of their multivalency, mPPCs achieve significantly higher inhibition and disassembly efficacy than corresponding amounts of monomeric LPFFD.[13,16,23] However, beyond an overall decrease in the aggregate size over time, details of the nanoscale processes involved in mPPC-induced disassembly observed in previous work were difficult to elucidate, in part because secondary structures (e.g., based on the CD spectroscopy results) were mostly unchanged in the process, with little discernible change over the disassembly time course.[16] With direct, high-resolution imaging, in this work we show that the disassembly of $A\beta_{40}$ fibrils by mPPCs proceeds not through dissolution or a simple "erosion" of fibril ends but through a sequence of fragmentation and lateral associations, leading to the formation of relatively uniform, platelike bundles. Quantitative statistical analysis of bundle size distributions indicates that fragmentation is a local process, with a rate constant independent of the fibril size and

geometry, suggesting specific interactions between amyloid fibrils and mPPCs rather than mechanically induced fragmentation. This observation differs from most synthetic disassembly pathways, which predominantly involve dissolution by small molecules[30−32] or mechanical agitation[19,20] of amyloid fibrils, and instead resembles the early stages of natural amyloid "disaggregase" behavior.[21] The bundling process, meanwhile, which was not resolved in previous investigations but revealed here at ~2 nm resolution, appears to exhibit a self-limiting behavior, which constrains the extent of lateral association to structures 3−5 fibrils wide. The overall β-sheet molecular ordering of the resulting bundles suggested by previous studies[16] was confirmed with nanobeam electron diffraction, while their platelike thickness was examined with electron tomography. Overall, these results provide a detailed, quantitative picture of how mPPCs are able to modulate the stability of amyloid fibrils. At the same time, the ability of mPPCs to direct the formation of amyloid nanostructures much more uniform than the starting amyloid fibrils has the potential for broader implications in the developing field of amyloid nanotechnology, where creating amyloid structures with well-defined size and structure is a major goal.[33−37]

■ RESULTS AND DISCUSSION

Disassembly of $A\beta_{40}$ fibrils was carried out as described previously,[16] and their morphological evolution at intervals before and after the addition of mPPCs was examined with negative-stain transmission electron microscopy (TEM; Figure
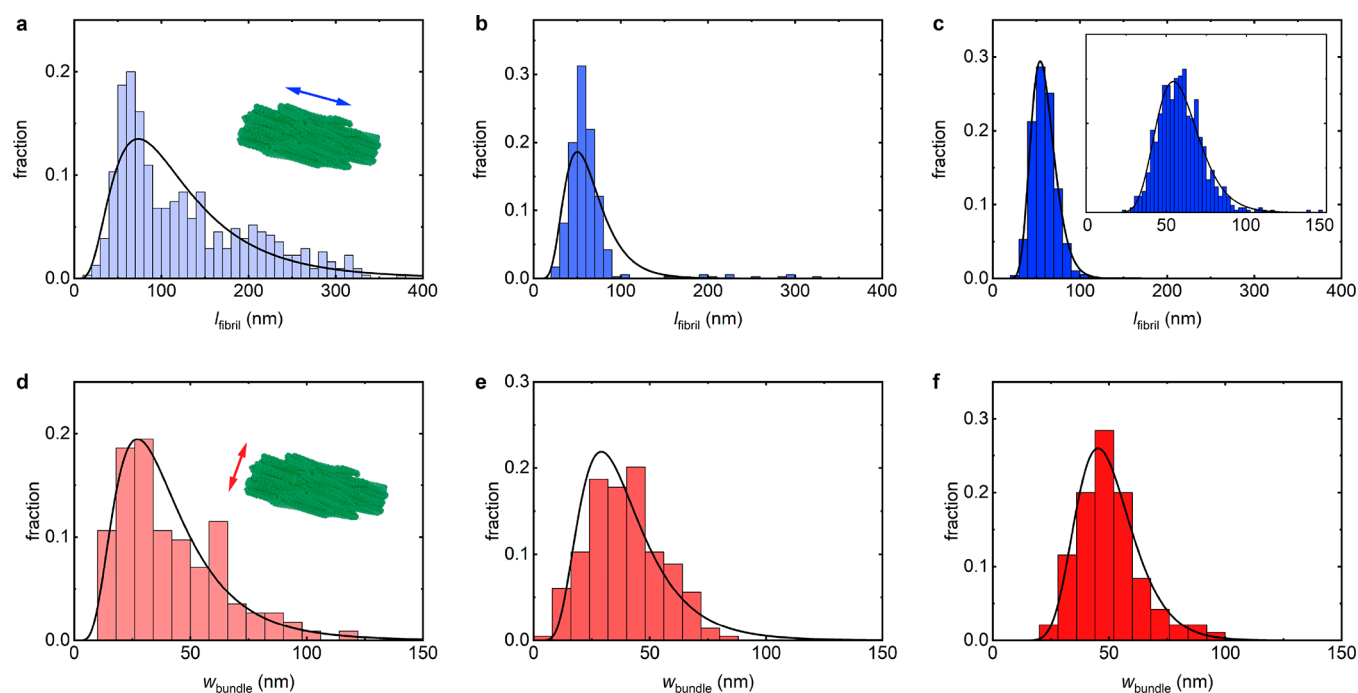
Figure 2. Fibril morphology evolution along the disassembly pathway. (a−c) From 24 (a), 48 (b), to 72 h (c) after the addition of mPPC to preassembled fibrils, the average fibril length l_{fibril} decreases from 130 to 67 nm at 48 h and to 59 nm within 72 h. The inset in part c shows a zoomed-in view of the 72 h l_{fibril} distribution highlighting the smaller size regime. (d−f) In parallel, lateral association of fibril segments leads to an increase of the average bundle width w_{bundle} from 23 nm at 24 h (d) to 50 nm within 72 h (f) after the addition of mPPC. All curves denote a best-fit log−normal distribution, as detailed in Figure 3.
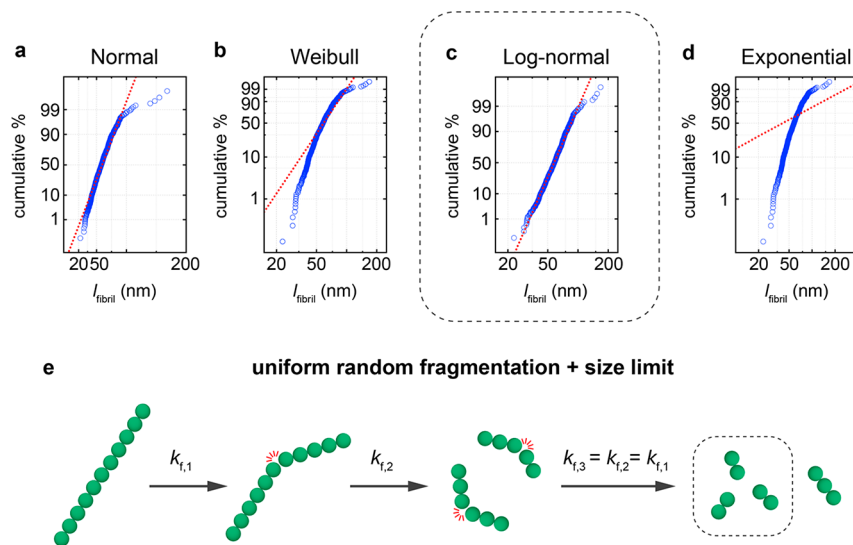
Figure 3. Fibril length dimensions that converge to a log−normal size distribution over time, indicating uniform random fragmentation. (a−d) Comparison of fits to the 72 h l_{fibril} cumulative probability distribution (Figure 2c), including the normal distribution (a), Weibull distribution (b), log−normal distribution (c), and exponential distribution (d). For comparison, the scales of the x and y axes are such that an ideal fit to the distribution would correspond to a straight line. The same data are shown on a linear scale in Figure S4 (see also Tables S1 and S2). (e) Schematic representation of uniform random fragmentation with a lower-bound size limit.

1). In brief, Aβ_{40} fibrils were prepared by dissolving 10 μM Aβ_{40} in a 10 mM phosphate buffer saline solution (pH 7.4) and applying linear shaking at 37 °C for 24 h. Separate solutions also containing ThT (10 μM) were incubated in the same 96-well plate to monitor fibril growth. On the basis of mass-per-length analysis[38−40] (Figure S1), assembled fibrils have on average a 2-fold symmetry, with two protofibrils wrapped around the fibril axis, consistent with previous studies using similar fibril growth conditions.[41] The helical twist of the

fibrils has a period $\gtrsim$200 nm, leading to variation of their projected widths between ∼8 and 30 nm (Figure S2). At the end of the fibril growth period (referred to as 0 h), mPPCs with a molecular weight of 90 kDa and a peptide loading of 7% (7 LPFFD-labeled units in every 100 units along the polymer) were added to bring the LPFFD−Aβ_{40} molar ratio to 32.5 and incubation was continued for 72 h thereafter, with samples being collected for examination in 24 h increments. Additional

details regarding the mPPC synthesis and experimental procedures can be found in the Supporting Information.

The addition of mPPCs leads to the disassembly of long, tangled $A\beta_{40}$ fibrils into much smaller, sub-100-nm structures (Figure 1a−d), whereas only minor structural changes are observed after 72 h without mPPC (Figure S3), consistent with previous studies.[16] More quantitatively, after the addition of mPPCs, fibrils shorten from an average length l_{fibril} = 269 nm at 0 h to 59 nm within 72 h (Figures 1e and 2a−c). In parallel, the standard deviation of the l_{fibril} distribution decreases dramatically—almost 10-fold—from 151 to 15 nm. This significant reduction of the distribution spread indicates that the underlying shortening pathway is not erosion from fibril ends but from fragmentation at multiple "break" points. At the same time, aided by the high-resolution morphological information provided by negative-stain TEM, additional details of the disassembly process were revealed. For example, as fragmentation occurs, we observed that $A\beta_{40}$ amyloid fibrils also associate laterally, forming bundles with width w_{bundle} = 50 ± 14 nm after 72 h with mPPC (Figures 1e and 2d−f). These nanoscopic aspects of the disassembly process were not apparent in our previous studies[16] because light scattering and AFM only revealed an overall reduction in the aggregate size after the addition of mPPCs to preformed fibrils. More importantly, these details reveal important mechanistic information.

For example, a detailed analysis of the l_{fibril} distribution during disassembly indicates that fibril shortening proceeds by uniform random fragmentation, with a rate constant independent of the fibril size or geometry. In particular, looking at the distributions of l_{fibril} in more detail, it is immediately apparent that fibril length distributions are highly asymmetric (Figure 2), with a Gaussian distribution providing a poor fit (Figure 3a and Tables S1 and S2). An overall asymmetric distribution of fibril lengths could have emerged from a variety of pathways, including (i) the equilibrium statistical mechanics of frangible rods,[42,43] (ii) steady-state behavior of kinetic master equations describing nucleated fibril growth in the presence of competing pathways,[24,43,44] or (iii) geometrically random one-dimensional fragmentation.[45,46] Each of these pathways, however, produces qualitative differences in the form of the size distribution that is produced, and our results are most consistent with the latter case. More specifically, for the first pathway, rate laws for linear assembly and disassembly can be derived directly and depend on the position of fracture and the length of the fracturing body.[42] Later it was shown that this geometry-dependent model produced length distributions with a form known as the Weibull distribution.[19,20] In the second pathway, which considers kinetic competition between processes in the assembly of breakable filaments (filament nucleation, monomer addition and dissociation, fragmentation, etc.), it was shown that a closed system will converge to positively skewed length distributions over time, with a shape that is only a function of the minimum stable nucleus size (details on the mathematical forms of these distributions are provided in the Supporting Information).[24,44] For the final model, it was derived that one-dimensional fragmentation with a rate constant *independent* of the aggregate size and a lower-bound size limit produces a positively skewed distribution known as the log−normal distribution.[45,47] In other words, convergence to this distribution indicates that fragmented fibrils are random fractions of the starting fibril length but have a lower bound on

their size (without a size limit, an exponential distribution of fragment sizes would emerge).

The observed l_{fibril} distributions are best described by the third model, i.e., the log−normal distribution (Figures 3a−d and S4), indicating a uniform random fragmentation process (Figure 3e). For example, using the l_{fibril} distribution at 72 h as an example, best-fit distributions to the Weibull and steady-state kinetic models fail to recapitulate the observed distribution of fibril sizes and instead tend to predict a much steeper drop in the distribution at the smallest fragment sizes (Figures 3a−d and S4). The log−normal distribution, on the other hand, can fit the observed distribution across the complete range of l_{fibril} and throughout the disassembly process. More quantitatively, both the Kolmogorov−Smirnov (Table S1) and Anderson−Darling (Table S2) goodness-of-fit test statistics, which measure the distance between the observed distribution and a particular best-fit distribution, consistently rank the log−normal distribution highest. This goodness-of-fit improves as disassembly progresses; at 72 h, the maximum deviation between the observed distribution and a log−normal distribution measured by the Kolmogorov−Smirnov test is as little as 0.03 (across 757 measurements; Table S1). Given the mechanistic underpinnings of the log−normal distribution and the inconsistency of the data with the Weibull and kinetic models that involve fibril geometry, this observation indicates that mPPC-induced fragmentation is a local process that does not depend on the position of fragmentation or the size of the breaking fibril (Figure 3e). This result is in contrast with amyloid fragmentation induced by mechanical agitation,[20] which instead produced a Weibull distribution of fragment sizes and is further supported by the magnitudes of the fragment lengths observed. For example, previous works have shown that $A\beta_{40}$ amyloid fibrils have persistence lengths in excess of several hundred nanometers;[48−50] the observed size distribution of l_{fibril} is far smaller than this characteristic mechanical length scale, as well as the twisting length scale of fibrils ($\gtrsim$200 nm; Figure S2). A "local" fragmentation mechanism points to a specific interaction between the mPPCs and amyloid fibrils, which is hypothesized to be encoded in the peptide ligands that they bear, and perhaps other physicochemical properties of mPPCs. For example, if fragmentation is the result of the interaction of an mPPC with local or transient defects along an amyloid fibril, or if binding of the mPPC peptide groups to the fibril structure leads to the formation of such defects, these interactions in the presence of peptide groups other than LPFFD could lead to different disassembly efficacies. These aspects are the subject of ongoing investigation.

In tandem with random fragmentation, shortened amyloid segments associate laterally and become highly aligned in bundles that are approximately 50 nm in width (Figure 2d−f). Interestingly, although short amyloid segments are produced at the very beginning of disassembly (some even as short as the l_{fibril} values after 72 h; Figure 2a) and begin to be incorporated into bundles 50 nm wide within 24 h (Figure 2d), further bundling is limited (i.e., segments or already associated bundles do not continue to associate side-to-side). From a colloidal standpoint, this result is surprising, for if broken amyloid fibrils behaved as simple attractive rods or cylinders, much larger structures would be expected within such an extended time frame. For example, attractive colloidal rods,[51,52] rodlike viruses[53,54] and other simple analogues tend to assemble to a much greater extent, sometimes to the point
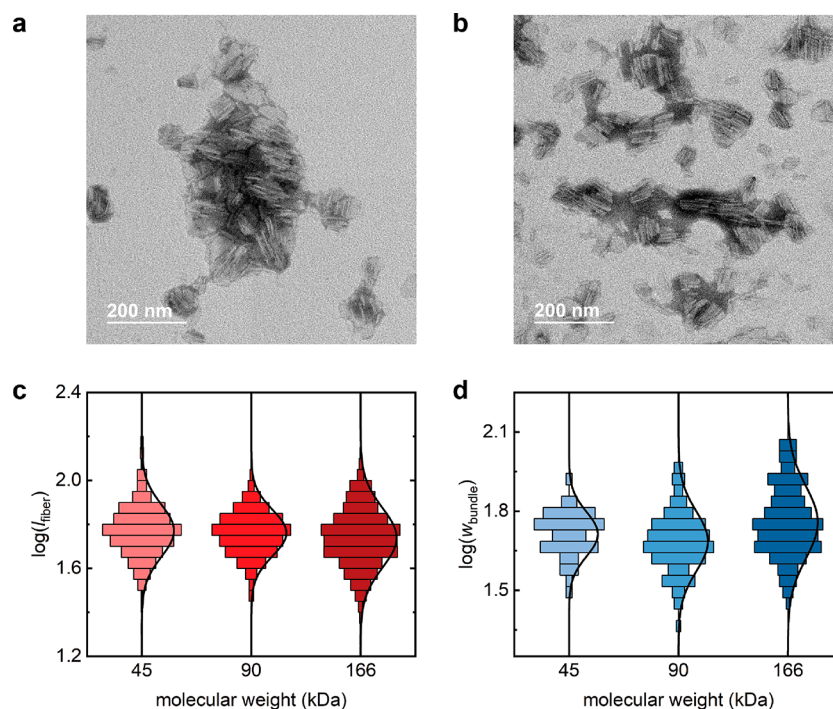
Figure 4. mPPCs with different molecular weights produce qualitatively and quantitatively similar bundles. (a−b) Representative negative-stain micrographs of bundles disassembled by (a) 45 kDa of mPPC and (b) 166 kDa of mPPC. The distributions of fibril lengths (c) and bundle widths (d) after 72 h of disassembly with increasing mPPC molecular weights are qualitatively and quantitatively consistent. See also Figures S5−S7. Both distributions are of the logarithm of their respective bundle dimensions to highlight their log−normal nature. Sample sizes for each data set are given in Tables S1 and S2.

of macroscopic phase separation. Similar to fragmentation, different means of self-limiting assembly have been proposed. One form has been observed in the assembly of stiff polyelectrolytes[55−58] like DNA,[59] but this requires complex electrostatic interactions and generally only takes place in the presence of multivalent cations, which are not present here. An alternative explanation that is more plausible here lies in the helicity of amyloid fibrils. In particular, the self-assembly of chiral filaments can also be self-limiting[60−63] because tight bundling such as that observed here requires the intrinsic twist of individual building blocks to change and thus accommodate elastic strain, which limits the lateral growth of helical bundles. Indeed, self-limiting bundling behavior has been observed in chiral protein filaments made of actin,[60] sickle-cell hemoglobin fibrils,[61,64] and other amyloid-like structures.[65,66] The facts that the observed bundles appear tightly aligned, with well-defined "stripes", and that the original (and control) long fibrils do not seem to bundle as easily (Figures 2b and S3j−l) is an indication of this elastic constraint. Analogously, a bundle of short amyloid segments should form more readily than a tight bundle of long amyloid fibrils. Future experiments on the disassembly of amyloid fibrils with well-defined twisting periodicity, such as polymorphs prepared using highly controlled amyloid assembly conditions, could elucidate more about such behavior. A second possible origin of this self-limiting effect is a delicate balance between the short-range attractive and long-range repulsive interactions[67,68] experienced by fibrils and fibril segments. In this system, attraction could come from van der Waals interactions, hydrophobic interactions, or attractions mediated by the mPPC, whereas repulsion originates from electrostatic interactions. In other systems, their interplay has been demonstrated to lead to self-limiting effects.[67,68]

Given the relative uniformity of amyloid bundles produced from mPPC-induced disassembly, we sought to investigate these structures in more detail. First, we repeated the disassembly experiments using mPPCs of both higher (166 kDa) and lower (45 kDa) molecular weights with the same 7% LPFFD peptide loading density. Previously, it was observed that higher-molecular-weight mPPCs tend to disassemble amyloid fibrils more rapidly, with the rate of disassembly being approximately linearly related to the overall concentration of peptide groups, with no observed critical concentration.[16] Surprisingly, the high-resolution imaging approach here revealed that while the mPPC molecular weight can influence the disassembly rate, fragmentation processes are not only qualitatively maintained (Figure 4a,b) but also produce *quantitatively* similar bundle geometries (Figures 4c,d and S5−S7; see Table S1 for the sample sizes). For example, not only does the distribution of l_{fibril} consistently converge to a log−normal distribution after 72 h (Figure 4c and Tables S1 and S2), indicating the same uniform fragmentation processes; different mPPCs also produce fibril segments of highly similar sizes, regardless of the mPPC molecular weight (53 ± 9 nm for 45 kDa, 50 ± 14 nm for 90 kDa, and 57 ± 19 nm for 166 kDa). The same behavior is seen in the case of bundling: regardless of the molecular weight, bundles form with w_{bundle} between 50 and 60 nm (Figure 4d). These consistencies corroborate many of the hypotheses about the underlying disassembly mechanisms—uniform fragmentation with self-limiting bundling—proposed above.

At the same time, we looked deeper into the bundle structures themselves. First, we endeavored to investigate the molecular-scale ordering of bundles to confirm that they maintain the characteristic structures of amyloid fibrils, as suggested in previous CD studies. Historically, X-ray or
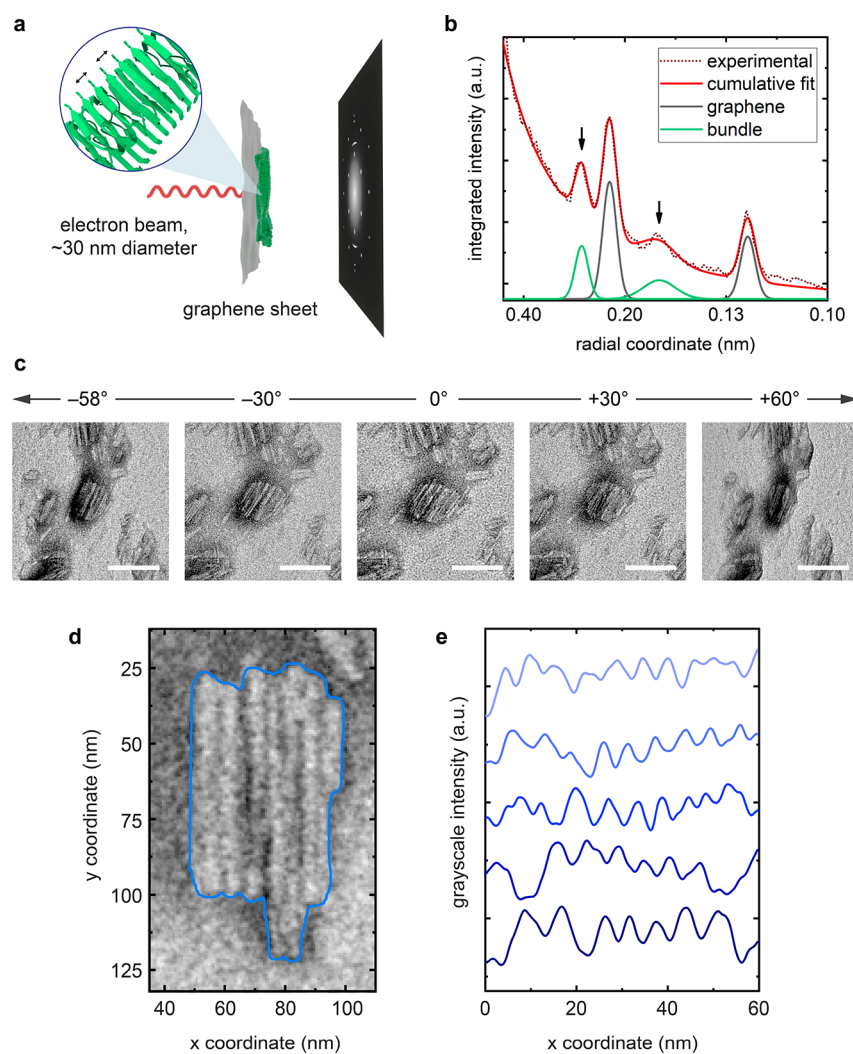
Figure 5. Structural analysis of the products of disassembly. (a) Schematic illustrating the internal β-sheet spacing (0.47 nm) characteristic of $A\beta_{40}$ amyloid fibrils. Bundles coming from disassembly by 90 kDa of mPPC after 72 h were chosen as representatives. (b) Radially integrated nanobeam electron diffraction pattern exhibiting higher-order peaks (0.24 and 0.16 nm) corresponding to the β-sheet spacing and to the graphene sheet used as a protective agent. (c) TEM images of a bundle collected from a wide range of tilt angles indicate that the thickness of the bundles is relatively small and the overall structure is platelike. (d) Magnified TEM image of a bundle resulting from the disassembly of amyloid fibrils, highlighting the well-defined "stripes". (e) Grayscale intensity integrated vertically along several different bundles, indicating a periodicity Δ of 6.2 $\pm$ 1.1 nm, consistent with protofibril length scales.

electron diffraction experiments have been used to "finger-print" amyloid structures.[69,70] However, these techniques require samples with large-scale ordering and alignment, which would make it difficult to probe scattering signatures locally and with certainty from nanoscale bundles. To circumvent these challenges, we used nanobeam electron diffraction, where diffraction patterns can be collected from regions a few tens of nanometers in diameter,[71] combined with electron damage mitigation using graphene (Figure 5a), to probe the structure of bundles. Figure 5b shows the resulting diffraction pattern taken from a single bundle structure and radially integrated. The pattern contains peaks corresponding to the graphene substrate (see also Figure S8) and higher-order peaks consistent with the 0.47 nm spacing, which has long served as a defining characteristic of amyloid fibrils.[69,72] To better understand the bundle structures in three dimensions, we collected TEM images of bundles from several different tilt angles (Figure 5c). The high-tilt images indicate that bundles are relatively platelike, extending only slightly into

the z direction and with thickness of $\lesssim$30 nm. Finally, we quantified the periodicity of bundle stripes (Figure 5d,e), which served as an additional indication of the underlying amyloid structure in that the average distance Δ between stripes (6.2 $\pm$ 1.1 nm) is consistent with the dimensions of the starting amyloid fibrils when they are twisted away from the TEM substrate (Figure S2b,d).

■ CONCLUSIONS

In summary, using a variety of electron microscopy techniques and quantitative image analysis, we have demonstrated that mPPCs induce the disassembly of $A\beta_{40}$ amyloid fibrils through a combination of fragmentation and bundling processes. Statistical analysis of the size evolution of fibrils and their assemblies provides evidence that mPPC-based fragmentation has a uniform, size- and position-independent rate, involving local interactions between fibrils and mPPCs and not merely mechanical agitation-induced breakage. Bundling, on the other hand, is a slow assembly process with a size-limiting behavior.

Collectively, these processes work together to produce uniform, ordered amyloid "rafts" regardless of the mPPC molecular weight, highlighting opportunities to create well-defined, molecularly ordered amyloid nanomaterials.

■ ASSOCIATED CONTENT

Ⓢ Supporting Information

The Supporting Information is available free of charge on the ACS Publications website at DOI: 10.1021/acsanm.9b01331.

Supplementary methods, Figures S1−S9, Tables S1 and S2, and supplementary references (PDF)

■ AUTHOR INFORMATION

Corresponding Authors

*E-mail: rienstra@illinois.edu.
*E-mail: jsmoore@illinois.edu.
*E-mail: qchen20@illinois.edu.

ORCID Ⓞ

Xing Jiang: 0000-0001-8259-1948
Hyosung An: 0000-0001-8710-1012
Giuseppe Licari: 0000-0002-8490-7536
Emad Tajkhorshid: 0000-0001-8434-1010
Chad M. Rienstra: 0000-0002-9912-5596
Jeffrey S. Moore: 0000-0001-5841-6269
Qian Chen: 0000-0002-1968-441X

Notes

The authors declare no competing financial interest.

■ ACKNOWLEDGMENTS

■ REFERENCES

(1) Cao, Q.; Shin, W. S.; Chan, H.; Vuong, C. K.; Dubois, B.; Li, B.; Murray, K. A.; Sawaya, M. R.; Feigon, J.; Black, D. L.; Eisenberg, D. S.; Jiang, L. Inhibiting Amyloid-β Cytotoxicity through Its Interaction with the Cell Surface Receptor LilrB2 by Structure-Based Design. *Nat. Chem.* **2018**, *10* (12), 1213−1221.

(2) Villemagne, V. L.; Doré, V.; Burnham, S. C.; Masters, C. L.; Rowe, C. C. Imaging Tau and Amyloid-β Proteinopathies in Alzheimer Disease and Other Conditions. *Nat. Rev. Neurol.* **2018**, *14* (4), 225−236.

(3) Tuttle, M. D.; Comellas, G.; Nieuwkoop, A. J.; Covell, D. J.; Berthold, D. A.; Kloepper, K. D.; Courtney, J. M.; Kim, J. K.; Barclay, A. M.; Kendall, A.; Wan, W.; Stubbs, G.; Schwieters, C. D.; Lee, V. M. Y.; George, J. M.; Rienstra, C. M. Solid-State NMR Structure of a Pathogenic Fibril of Full-Length Human α-Synuclein. *Nat. Struct. Mol. Biol.* **2016**, *23* (5), 409−415.

(4) Westermark, P.; Engström, U.; Johnson, K. H.; Westermark, G. T.; Betsholtz, C. Islet Amyloid Polypeptide: Pinpointing Amino Acid Residues Linked to Amyloid Fibril Formation. *Proc. Natl. Acad. Sci. U. S. A.* **1990**, *87* (13), 5036−5040.

(5) Van Gerven, N.; Klein, R. D.; Hultgren, S. J.; Remaut, H. Bacterial Amyloid Formation: Structural Insights into Curli Biogensis. *Trends Microbiol.* **2015**, *23* (11), 693−706.

(6) Barnhart, M. M.; Chapman, M. R. Curli Biogenesis and Function. *Annu. Rev. Microbiol.* **2006**, *60* (1), 131−147.

(7) Wosten, H.; De Vries, O.; Wessels, J. Interfacial Self-Assembly of a Fungal Hydrophobin into a Hydrophobic Rodlet Layer. *Plant Cell* **1993**, *5* (11), 1567−1574.

(8) Claessen, D.; Stokroos, I.; Deelstra, H. J.; Penninga, N. A.; Bormann, C.; Salas, J. A.; Dijkhuizen, L.; Wösten, H. A. B. The Formation of the Rodlet Layer of Streptomycetes Is the Result of the Interplay between Rodlins and Chaplins. *Mol. Microbiol.* **2004**, *53* (2), 433−443.

(9) Nespovitaya, N.; Gath, J.; Barylyuk, K.; Seuring, C.; Meier, B. H.; Riek, R. Dynamic Assembly and Disassembly of Functional β-Endorphin Amyloid Fibrils. *J. Am. Chem. Soc.* **2016**, *138* (3), 846−856.

(10) Selkoe, D. J.; Hardy, J. The Amyloid Hypothesis of Alzheimer's Disease at 25 Years. *EMBO Mol. Med.* **2016**, *8* (6), 595−608.

(11) Hardy, J.; Selkoe, D. J. The Amyloid Hypothesis of Alzheimer's Disease: Progress and Problems on the Road to Therapeutics. *Science* **2002**, *297* (5580), 353−356.

(12) Honig, L. S.; Vellas, B.; Woodward, M.; Boada, M.; Bullock, R.; Borrie, M.; Hager, K.; Andreasen, N.; Scarpini, E.; Liu-Seifert, H.; Case, M.; Dean, R. A.; Hake, A.; Sundell, K.; Poole Hoffmann, V.; Carlson, C.; Khanna, R.; Mintun, M.; DeMattos, R.; Selzler, K. J.; Siemers, E. Trial of Solanezumab for Mild Dementia Due to Alzheimer's Disease. *N. Engl. J. Med.* **2018**, *378* (4), 321−330.

(13) Song, Y.; Cheng, P.-N.; Zhu, L.; Moore, E. G.; Moore, J. S. Multivalent Macromolecules Redirect Nucleation-Dependent Fibrillar Assembly into Discrete Nanostructures. *J. Am. Chem. Soc.* **2014**, *136* (14), 5233−5236.

(14) Crespo, R.; Villar-Alvarez, E.; Taboada, P.; Rocha, F. A.; Damas, A. M.; Martins, P. M. What Can the Kinetics of Amyloid Fibril Formation Tell about Off-Pathway Aggregation? *J. Biol. Chem.* **2016**, *291* (4), 2018−2032.

(15) Arosio, P.; Knowles, T. P. J.; Linse, S. On the Lag Phase in Amyloid Fibril Formation. *Phys. Chem. Chem. Phys.* **2015**, *17* (12), 7606−7618.

(16) Song, Y.; Moore, E. G.; Guo, Y.; Moore, J. S. Polymer−Peptide Conjugates Disassemble Amyloid β Fibrils in a Molecular-Weight Dependent Manner. *J. Am. Chem. Soc.* **2017**, *139* (12), 4298−4301.

(17) Michaels, T. C. T.; Dear, A. J.; Knowles, T. P. J. Scaling and Dimensionality in the Chemical Kinetics of Protein Filament Formation. *Int. Rev. Phys. Chem.* **2016**, *35* (4), 679−703.

(18) Xue, W.-F.; Hellewell, A. L.; Gosal, W. S.; Homans, S. W.; Hewitt, E. W.; Radford, S. E. Fibril Fragmentation Enhances Amyloid Cytotoxicity. *J. Biol. Chem.* **2009**, *284* (49), 34272−34282.

(19) Xue, W.-F.; Homans, S. W.; Radford, S. E. Amyloid Fibril Length Distribution Quantified by Atomic Force Microscopy Single-Particle Image Analysis. *Protein Eng., Des. Sel.* **2009**, *22* (8), 489−496.

(20) Xue, W.-F.; Radford, S. E. An Imaging and Systems Modeling Approach to Fibril Breakage Enables Prediction of Amyloid Behavior. *Biophys. J.* **2013**, *105* (12), 2811−2819.

(21) Gao, X.; Carroni, M.; Nussbaum-Krammer, C.; Mogk, A.; Nillegoda, N. B.; Szlachcic, A.; Guilbride, D. L.; Saibil, H. R.; Mayer, M. P.; Bukau, B. Human Hsp70 Disaggregase Reverses Parkinson's-Linked α-Synuclein Amyloid Fibrils. *Mol. Cell* **2015**, *59* (5), 781−793.

(22) Xu, Y.; Safari, M. S.; Ma, W.; Schafer, N. P.; Wolynes, P. G.; Vekilov, P. G. Steady, Symmetric, and Reversible Growth and Dissolution of Individual Amyloid-β Fibrils. *ACS Chem. Neurosci.* **2019**, *10* (6), 2967−2976.

(23) Chafekar, S. M.; Malda, H.; Merkx, M.; Meijer, E. W.; Viertl, D.; Lashuel, H. A.; Baas, F.; Scheper, W. Branched KLVFF Tetramers Strongly Potentiate Inhibition of β-Amyloid Aggregation. *ChemBioChem* **2007**, *8* (15), 1857−1864.

(24) Cohen, S. I. A.; Vendruscolo, M.; Dobson, C. M.; Knowles, T. P. J. Nucleated Polymerization with Secondary Pathways. III.

Equilibrium Behavior and Oligomer Populations. *J. Chem. Phys.* **2011**, *135* (6), No. 065107.

(25) Xu, H.; Shaw, D. E. A Simple Model of Multivalent Adhesion and Its Application to Influenza Infection. *Biophys. J.* **2016**, *110* (1), 218−233.

(26) Krishnamurthy, V. M.; Estroff, L. A.; Whitesides, G. M. Multivalency in Ligand Design. *Fragment-based Approaches in Drug Discovery*; John Wiley & Sons, Ltd., 2006; pp 11−53.

(27) Carlini, A. S.; Adamiak, L.; Gianneschi, N. C. Biosynthetic Polymers as Functional Materials. *Macromolecules* **2016**, *49* (12), 4379−4394.

(28) Murvai, Ü.; Soós, K.; Penke, B.; Kellermayer, M. S. Z. Effect of the Beta-Sheet-Breaker Peptide LPFFD on Oriented Network of Amyloid B25−35 Fibrils. *J. Mol. Recognit.* **2011**, *24* (3), 453−460.

(29) Yang, C.; Zhu, X.; Li, J.; Shi, R. Exploration of the Mechanism for LPFFD Inhibiting the Formation of β-Sheet Conformation of Aβ(1−42) in Water. *J. Mol. Model.* **2010**, *16* (4), 813−821.

(30) Bieschke, J.; Russ, J.; Friedrich, R. P.; Ehrnhoefer, D. E.; Wobst, H.; Neugebauer, K.; Wanker, E. E. EGCG Remodels Mature α-Synuclein and Amyloid-β Fibrils and Reduces Cellular Toxicity. *Proc. Natl. Acad. Sci. U. S. A.* **2010**, *107* (17), 7710−7715.

(31) Blanchard, B. J.; Chen, A.; Rozeboom, L. M.; Stafford, K. A.; Weigele, P.; Ingram, V. M. Efficient Reversal of Alzheimer's Disease Fibril Formation and Elimination of Neurotoxicity by a Small Molecule. *Proc. Natl. Acad. Sci. U. S. A.* **2004**, *101* (40), 14326−14332.

(32) Han, Y.; He, C.; Cao, M.; Huang, X.; Wang, Y.; Li, Z. Facile Disassembly of Amyloid Fibrils Using Gemini Surfactant Micelles. *Langmuir* **2010**, *26* (3), 1583−1587.

(33) Wei, G.; Su, Z.; Reynolds, N. P.; Arosio, P.; Hamley, I. W.; Gazit, E.; Mezzenga, R. Self-Assembling Peptide and Protein Amyloids: From Structure to Tailored Function in Nanotechnology. *Chem. Soc. Rev.* **2017**, *46* (15), 4661−4708.

(34) Shen, Y.; Posavec, L.; Bolisetty, S.; Hilty, F. M.; Nyström, G.; Kohlbrecher, J.; Hilbe, M.; Rossi, A.; Baumgartner, J.; Zimmermann, M. B.; Mezzenga, R. Amyloid Fibril Systems Reduce, Stabilize and Deliver Bioavailable Nanosized Iron. *Nat. Nanotechnol.* **2017**, *12* (7), 642−647.

(35) Mankar, S.; Anoop, A.; Sen, S.; Maji, S. K. Nanomaterials: Amyloids Reflect Their Brighter Side. *Nano Rev.* **2011**, *2* (1), 6032.

(36) Cherny, I.; Gazit, E. Amyloids: Not Only Pathological Agents but Also Ordered Nanomaterials. *Angew. Chem., Int. Ed.* **2008**, *47* (22), 4062−4069.

(37) Ku, T.-H.; Sahu, S.; Kosa, N. M.; Pham, K. M.; Burkart, M. D.; Gianneschi, N. C. Tapping a Bacterial Enzymatic Pathway for the Preparation and Manipulation of Synthetic Nanomaterials. *J. Am. Chem. Soc.* **2014**, *136* (50), 17378−17381.

(38) Sen, A.; Baxa, U.; Simon, M. N.; Wall, J. S.; Sabate, R.; Saupe, S. J.; Steven, A. C. Mass Analysis by Scanning Transmission Electron Microscopy and Electron Diffraction Validate Predictions of Stacked β-Solenoid Model of HET-s Prion Fibrils. *J. Biol. Chem.* **2007**, *282* (8), 5545−5550.

(39) Ksiezak-Reding, H.; Wall, J. S. Characterization of Paired Helical Filaments by Scanning Transmission Electron Microscopy. *Microsc. Res. Tech.* **2005**, *67* (3−4), 126−140.

(40) Chen, B.; Thurber, K. R.; Shewmaker, F.; Wickner, R. B.; Tycko, R. Measurement of Amyloid Fibril Mass-per-Length by Tilted-Beam Transmission Electron Microscopy. *Proc. Natl. Acad. Sci. U. S. A.* **2009**, *106* (34), 14339−14344.

(41) Tycko, R. Molecular Structure of Aggregated Amyloid-β: Insights from Solid-State Nuclear Magnetic Resonance. *Cold Spring Harbor Perspect. Med.* **2016**, *6* (8), a024083.

(42) Hill, T. L. Length Dependence of Rate Constants for End-to-End Association and Dissociation of Equilibrium Linear Aggregates. *Biophys. J.* **1983**, *44* (2), 285−288.

(43) Schreck, J. S.; Yuan, J.-M. A Kinetic Study of Amyloid Formation: Fibril Growth and Length Distributions. *J. Phys. Chem. B* **2013**, *117* (21), 6574−6583.

(44) Michaels, T. C. T.; Yde, P.; Willis, J. C. W.; Jensen, M. H.; Otzen, D.; Dobson, C. M.; Buell, A. K.; Knowles, T. P. J. The Length Distribution of Frangible Biofilaments. *J. Chem. Phys.* **2015**, *143* (16), 164901.

(45) Koch, A. L. The Logarithm in Biology 1. Mechanisms Generating the Log-Normal Distribution Exactly. *J. Theor. Biol.* **1966**, *12* (2), 276−290.

(46) Grönholm, T.; Annila, A. Natural Distribution. *Math. Biosci.* **2007**, *210* (2), 659−667.

(47) Tenchov, B. G.; Yanev, T. K. Weibull Distribution of Particle Sizes Obtained by Uniform Random Fragmentation. *J. Colloid Interface Sci.* **1986**, *111* (1), 1−7.

(48) Sweers, K. K. M.; Bennink, M. L.; Subramaniam, V. Nanomechanical Properties of Single Amyloid Fibrils. *J. Phys.: Condens. Matter* **2012**, *24* (24), 243101.

(49) Choi, B.; Kim, T.; Lee, S. W.; Eom, K. Nanomechanical Characterization of Amyloid Fibrils Using Single-Molecule Experiments and Computational Simulations. https://www.hindawi.com/journals/jnm/2016/5873695/ (accessed June 6, 2019).

(50) Schleeger, M.; vandenAkker, C. C.; Deckert-Gaudig, T.; Deckert, V.; Velikov, K. P.; Koenderink, G.; Bonn, M. Amyloids: From Molecular Structure to Mechanical Properties. *Polymer* **2013**, *54* (10), 2473−2488.

(51) Yu, X.; Carlsson, A. E. Kinetics of Filament Bundling with Attractive Interactions. *Biophys. J.* **2004**, *87* (6), 3679−3689.

(52) Wilkins, G. M. H.; Spicer, P. T.; Solomon, M. J. Colloidal System To Explore Structural and Dynamical Transitions in Rod Networks, Gels, and Glasses. *Langmuir* **2009**, *25* (16), 8951−8959.

(53) Huang, F.; Rotstein, R.; Fraden, S.; Kasza, K. E.; Flynn, N. T. Phase Behavior and Rheology of Attractive Rod-like Particles. *Soft Matter* **2009**, *5* (14), 2766−2771.

(54) Zhang, Z.; Krishna, N.; Lettinga, M. P.; Vermant, J.; Grelet, E. Reversible Gelation of Rod-Like Viruses Grafted with Thermoresponsive Polymers. *Langmuir* **2009**, *25* (4), 2437−2442.

(55) Fazli, H.; Golestanian, R. Aggregation Kinetics of Stiff Polyelectrolytes in the Presence of Multivalent Salt. *Phys. Rev. E* **2007**, *76* (4), No. 041801.

(56) Stevens, M. J. Bundle Binding in Polyelectrolyte Solutions. *Phys. Rev. Lett.* **1999**, *82* (1), 101−104.

(57) Lee, K.-C.; Borukhov, I.; Gelbart, W. M.; Liu, A. J.; Stevens, M. J. Effect of Mono- and Multivalent Salts on Angle-Dependent Attractions Between Charged Rods. *Phys. Rev. Lett.* **2004**, *93* (12), 128101.

(58) Limbach, H. J.; Sayar, M.; Holm, C. Polyelectrolyte Bundles. *J. Phys.: Condens. Matter* **2004**, *16* (22), S2135−S2144.

(59) Ha, B.-Y.; Liu, A. J. Kinetics of Bundle Growth in DNA Condensation. *EPL Europhys. Lett.* **1999**, *46* (5), 624.

(60) Yang, Y.; Meyer, R. B.; Hagan, M. F. Self-Limited Self-Assembly of Chiral Filaments. *Phys. Rev. Lett.* **2010**, *104* (25), 258102.

(61) Turner, M. S.; Briehl, R. W.; Ferrone, F. A.; Josephs, R. Twisted Protein Aggregates and Disease: The Stability of Sickle Hemoglobin Fibers. *Phys. Rev. Lett.* **2003**, *90* (12), 128103.

(62) Grason, G. M.; Bruinsma, R. F. Chirality and Equilibrium Biopolymer Bundles. *Phys. Rev. Lett.* **2007**, *99* (9), No. 098101.

(63) Hosek, M.; Tang, J. X. Polymer-Induced Bundling of F Actin and the Depletion Force. *Phys. Rev. E* **2004**, *69* (5), No. 051907.

(64) Lu, L.; Li, X.; Vekilov, P. G.; Karniadakis, G. E. Probing the Twisted Structure of Sickle Hemoglobin Fibers via Particle Simulations. *Biophys. J.* **2016**, *110* (9), 2085−2093.

(65) Knowles, T. P. J.; De Simone, A.; Fitzpatrick, A. W.; Baldwin, A.; Meehan, S.; Rajah, L.; Vendruscolo, M.; Welland, M. E.; Dobson, C. M.; Terentjev, E. M. Twisting Transition between Crystalline and Fibrillar Phases of Aggregated Peptides. *Phys. Rev. Lett.* **2012**, *109* (15), 158101.

(66) Aggeli, A.; Nyrkova, I. A.; Bell, M.; Harding, R.; Carrick, L.; McLeish, T. C. B.; Semenov, A. N.; Boden, N. Hierarchical Self-Assembly of Chiral Rod-like Molecules as a Model for Peptide β-Sheet Tapes, Ribbons, Fibrils, and Fibers. *Proc. Natl. Acad. Sci. U. S. A.* **2001**, *98* (21), 11857−11862.

(67) Xia, Y.; Nguyen, T. D.; Yang, M.; Lee, B.; Santos, A.; Podsiadlo, P.; Tang, Z.; Glotzer, S. C.; Kotov, N. A. Self-Assembly of Self-Limiting Monodisperse Supraparticles from Polydisperse Nanoparticles. *Nat. Nanotechnol.* **2011**, *6* (9), 580−587.

(68) Yang, M.; Chan, H.; Zhao, G.; Bahng, J. H.; Zhang, P.; Král, P.; Kotov, N. A. Self-Assembly of Nanoparticles into Biomimetic Capsid-like Nanoshells. *Nat. Chem.* **2017**, *9* (3), 287−294.

(69) Serpell, L. C.; Fraser, P. E.; Sunde, M. [34] X-Ray Fiber Diffraction of Amyloid Fibrils.*Methods in Enzymology; Amyloid, Prions, and Other Protein Aggregates*; Academic Press, 1999; Vol. *309*, pp 526−536. .

(70) Eisenberg, D. S.; Sawaya, M. R. Structural Studies of Amyloid Proteins at the Molecular Level. *Annu. Rev. Biochem.* **2017**, *86* (1), 69−95.

(71) Zuo, J. M.; Gao, M.; Tao, J.; Li, B. Q.; Twesten, R.; Petrov, I. Coherent Nano-Area Electron Diffraction. *Microsc. Res. Tech.* **2004**, *64* (5−6), 347−355.

(72) Sunde, M.; Blake, C. The Structure of Amyloid Fibrils by Electron Microscopy and X-Ray Diffraction. In *Advances in Protein Chemistry*; Richards, F. M., Eisenberg, D. S., Kim, P. S., Eds.; Protein Misassembly; Academic Press, 1997; Vol. *50*, pp 123−159.